



Dry reforming of methane over bimetallic Ni-Co catalyst prepared from La_{(Co_xNi_{1-x})_{0.5}Fe_{0.5}O₃} perovskite precursor: Catalytic activity and coking resistance}



Haiqian Wang*, Xiaolei Dong, Tingting Zhao, Haoran Yu, Ming Li

Hefei National Laboratory for Physical Sciences at the Microscale, University of Science and Technology of China, Hefei, Anhui 230026, People's Republic of China

ARTICLE INFO

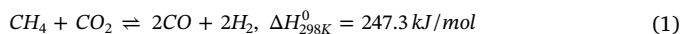
Keywords:
Bimetallic Ni-Co catalyst
Perovskite structure
Dry reforming of methane

ABSTRACT

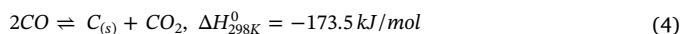
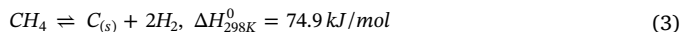
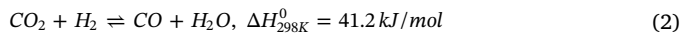
Exploring highly active Ni based catalysts with high coking resistance is of great importance for dry reforming of methane. Bimetallic Ni-Co catalysts supported on La₂O₃-LaFeO₃ were prepared by reducing La_{(Co_xNi_{1-x})_{0.5}Fe_{0.5}O₃} perovskite precursors. The perovskite precursors adopt orthorhombic, rhombohedral crystalline structure, or both, depending on the Co content. The catalytic activity and coking resistance are obviously enhanced by substituting a proper amount of Co, which should be essentially attributed to the synergistic effect between Ni and Co. Interestingly, the crystalline structure of the perovskite also plays an important role. Catalysts reduced from orthorhombic perovskite precursors with $x = 0.10$ and 0.30 have obvious higher structural stability, which show maximal catalytic activity and coking resistance. The multiple valences and spin states features of Co cations may affect the stability of the perovskite structure, and thus affect the active oxygen species in the perovskite, which promote both the catalytic activity and the removal of deposited carbon species.}

1. Introduction

Dry reforming of methane (DRM) attracts considerable attention recently because it converts two important greenhouse gases to valuable syngas with H₂/CO close to one, which is preferred for synthesizing important hydrocarbons through Fischer-Tropsch reaction [1,2]. The main reaction of DRM [3,4] is



Accompanying this, there are also a few side reactions, such as the reverse water-gas shift (RWGS) reaction, CH₄ decomposition reaction, and Boudouard reaction, which can be formulated respectively as [3,4]:



The DRM reaction (Eq. (1)) needs to be carried out at a high temperature due to its endothermic nature. The RWGS reaction reduces the H₂/CO ratio to below one, while the CH₄ decomposition (Eq. (3)) and Boudouard (Eq. (4)) reactions may bring serious carbon deposition problems.

Ni is abundant and low-cost relative to noble metals. It shows reasonably high catalytic activity among the transition metals, and thus appears to be one of the most important catalysts for DRM reactions [1,2,5,6]. However, Ni based catalysts tend to deactivate due to coking. Many efforts have been paid to explore highly active Ni based catalysts with good coking resistance, which include decreasing the metallic particle size, improving Ni particle distribution and enhancing the metal-support interaction [1,2,7,8]. On the other hand, it is proved that DRM reactions are quite sensitive to the surface structure of Ni particles [1,9]. Thus, tailoring the Ni surface structure by alloying Ni with another metal is an effective way to develop high performance catalysts. It is reported that bimetallic Ni based catalysts, such as Ni-Co alloy catalysts, show high activity and high coking resistance due to the strong oxygen affinity of Co and the synergistic effect between the different metallic components [1,10,11]. For example, Ni-Co-Al-Mg-O catalysts prepared by co-precipitation method [12] and Co-Ni-Mg-O catalysts prepared by hydrothermal method [13] show very good performances in terms of catalytic activity and coking resistance. Bimetallic Ni-Co catalysts can also be prepared from perovskite type precursors. Comparing to the traditional co-precipitation method, preparing bimetallic catalysts by using perovskites as precursors is more effective in terms of obtaining homogeneously distributed bimetallic particles and avoiding the existence of monometallic particles [14]. Bimetallic catalysts with

* Corresponding author.

E-mail address: hqwang@ustc.edu.cn (H. Wang).

Ni-Co alloy nanoparticles well dispersed on La_2O_3 (and/or $\text{La}_2\text{O}_2\text{CO}_3$) support have been prepared by reducing $\text{LaCo}_x\text{Ni}_{1-x}\text{O}_3$ perovskite precursors, which present high activity and coking resistance for the reactions of DRM and steam reforming of ethanol [5,14–16].

The catalytic performances of Ni-based catalysts depend not only on the metallic components, but also on the supports. It is demonstrated that a perovskite support may affect the activity and coking resistance of Ni based catalysts, which is attributed to the strong metal-support interaction, high oxygen mobility in the perovskite, or even the self-regeneration effect of the perovskite [4,14,17–19]. However, perovskite precursors like LaNiO_3 , LaCoO_3 or $\text{LaCo}_x\text{Ni}_{1-x}\text{O}_3$ are not stable under H_2 reduction and/or DRM conditions, and fully decompose into metallic particles and La_2O_3 or $\text{La}_2\text{O}_2\text{CO}_3$ [5,14–16,20]. Partial substitution of Fe at the B-site of these perovskites is an effective way to stabilize the perovskite structure under DRM conditions and improve the performance of the catalysts. It is reported that partial substitution of Fe at the B-site of LaNiO_3 greatly reduces the rate of coke buildup, but the catalytic activity is reduced to a lower level [4,21]. The improved coking resistance is mainly attributed to the enhanced metal-support interaction and the active oxygen species in the Fe-stabilized perovskite. Wang et al. [22] reported that Ni-Co/ LaFeO_3 - La_2O_3 catalysts prepared by reducing $\text{LaFe}_{1-x-y}\text{Ni}_x\text{Co}_y\text{O}_3$ show excellent resistance to coking, and the Ni-Co nanoparticles are in the state of solid solution alloy. In a recent work, we have demonstrated that the $(\text{LaCe})(\text{NiFe})\text{O}_3$ perovskite structure which is stable under DRM conditions also promotes the activity of Ni based catalyst through an oxygen vacancy mechanism and/or a redox mechanism [17].

The importance of perovskite structure on the catalytic performance has been found in different reactions. For example, Pecchi et al. [23] reported that the perovskite structure of $\text{LaMn}_{0.9}\text{Co}_{0.1}\text{O}_3$ can be tuned from rhombohedral to orthorhombic by partial substitution of La with Ag, and the orthorhombic structure is more active for catalyzing the n-hexane combustion reaction. Bedel et al. [24] reported that the crystalline structure of $\text{LaCo}_x\text{Fe}_{1-x}\text{O}_3$ can be tuned from orthorhombic to rhombohedral by increasing the Co content, and interestingly, only the orthorhombic structure is active for Fischer-Tropsch synthesis. The authors proposed that the orthorhombic structure is stable even with a high number of cation vacancies, and thus facilitates the reduction of Co^{3+} to Co^0 , which is well dispersed on the cation-deficient perovskite support. An ideal perovskite with the general formula of ABO_3 has cubic crystalline structure and belongs to space group of $\text{Pm}3\text{m}$. In real cases, the crystalline structure of a perovskite may change from cubic to orthogonal and rhombohedral etc., depending on the degree of the lattice distortion induced from the cooperative rotation of the corner-sharing BO_6 octahedra around its center [25]. Moreover, the rotation of the BO_6 octahedra changes the B–O bond length and the B–O–B angle, thus influences the stability, electronic structure and catalytic properties [25,26]. In addition to synergistic effect and metal-support interaction, it is also interesting to examine the effect of perovskite structure on the catalytic performance for DRM reactions.

In the present work, bimetallic Ni-Co catalysts supported on La_2O_3 - LaFeO_3 for DRM were prepared by reducing $\text{La}(\text{Co}_x\text{Ni}_{1-x})_{0.5}\text{Fe}_{0.5}\text{O}_3$ ($x = 0.0\text{--}1.0$) perovskite precursors. We found that the catalytic performances in terms of catalytic activity and coking resistance strongly depend on the Co content. Interestingly, the crystalline structure of the perovskites, which can be tuned by the Co content, has an important effect on the catalytic activity and coking resistance.

2. Experimental

2.1. Catalyst preparation

$\text{La}(\text{Co}_x\text{Ni}_{1-x})_{0.5}\text{Fe}_{0.5}\text{O}_3$ catalyst precursors were synthesized by sol-gel self-combustion method. Citric acid monohydrate ($\text{C}_6\text{H}_8\text{O}_7 \cdot \text{H}_2\text{O}$) was used as the complexing agent. Lanthanum oxide (La_2O_3), cobalt nitrate hexahydrate ($\text{Co}(\text{NO}_3)_2 \cdot 6\text{H}_2\text{O}$), nickel nitrate hexahydrate ($\text{Ni}(\text{NO}_3)_2 \cdot 6\text{H}_2\text{O}$), and ferric nitrate nonahydrate ($\text{Fe}(\text{NO}_3)_3 \cdot 9\text{H}_2\text{O}$) were used as the starting materials. All the chemicals (analytical grade) were purchased from Sinopharm Chemical Agent Company.

La_2O_3 was dissolved in distilled water, and nitric acid was added under constant stirring. Then, proper amount of $\text{Fe}(\text{NO}_3)_3 \cdot 9\text{H}_2\text{O}$, $\text{Co}(\text{NO}_3)_3 \cdot 6\text{H}_2\text{O}$ and $\text{Ni}(\text{NO}_3)_2 \cdot 6\text{H}_2\text{O}$ were added successively into the $\text{La}(\text{NO}_3)_3$ solution under stirring. The aqueous solution was stirred at 50 °C for 1 h, and then citric acid monohydrate was added. The proportion between citric acid monohydrate and the metal ions was set as 1.25:1. The pH value of the solution was adjusted to 8 by adding ammonia solution (25% NH_3 by weight in water). After stirring at 50 °C for 24 h, the solution was heated on an electric furnace until ignited. The spongy material was collected and calcined at 700 °C for 5 h to remove residual carbon. The obtained catalyst precursors were in the powder form.

For the convenience of discussion, we denote the samples by the Co content (x) in $\text{La}(\text{Co}_x\text{Ni}_{1-x})_{0.5}\text{Fe}_{0.5}\text{O}_3$. The two end members, $\text{LaNi}_{0.5}\text{Fe}_{0.5}\text{O}_3$ and $\text{LaCo}_{0.5}\text{Fe}_{0.5}\text{O}_3$, are also named as LNF and LCF, respectively.

2.2. Characterization

The crystalline phase structure of the powder samples was examined by an X-ray diffractometer (XRD, MXPAHF, MacScience) using Cu K α radiation over the range of $2\theta = 20^\circ\text{--}80^\circ$ at room temperature. X-ray photoelectron spectroscopy (XPS) analysis was performed by using an electron spectrometer (ESCALAB 250, Thermo-VG Scientific, U.S.). The morphology of the samples was observed by scanning electron microscopy (SEM, JSM-6700 F, JEOL) and transmission electron microscopy (TEM, JEM-2011, JEOL, Japan).

The BET surface areas were measured by nitrogen sorption at liquid nitrogen temperature (77 K) by using a surface area analyzer (Quantachrome NOVA 3200e). Prior to N_2 adsorption, the samples were degassed at 300 °C for 2 h to remove any residual moisture and other volatiles.

Temperature programmed reduction (TPR) was carried out with a simultaneous thermal analyzer (STA449F3, NETZSCH, Germany). 10–15 mg powder sample was placed in an alumina crucible and heated from room temperature to 1200 °C with a heating rate of 10 °C/min. The flow rate of the forming gas (5 vol% H_2/N_2) was 60 sccm.

Temperature programmed oxidation (TPO) was performed on the used catalysts to analyze the carbon deposition. The analysis was carried out with a simultaneous thermal analyzer (STA 449 F3, NETZSCH, Germany). 10–15 mg powder sample was placed in an alumina crucible. The sample was firstly heated under 10 sccm N_2 protection to 800 °C with a heating rate of 10 °C/min to remove adsorbed gas molecules and to decompose $\text{La}_2\text{O}_2\text{CO}_3$. After being cooled down to room temperature, the sample was again heated to 950 °C in dry air with a heating rate of 10 °C/min. The weight loss detected in the high temperature stage reflects the amount of deposited carbon.

2.3. Catalyst activity test

300 mg sample was placed in a fixed bed quartz reactor (i.d. = 6 mm) without dilution, except when otherwise specified. The sample was reduced in pure H_2 at 700 °C for 2 h before test. After purging by N_2 for 30 min, the reactor was heated to the test temperature under a continuous feed of equimolecular CO_2/CH_4 mixture with a flow rate of 60 mL/min without dilution. The same gaseous hourly space velocity (GHSV) of $1.2 \times 10^4 \text{ mL g}^{-1} \text{ h}^{-1}$ (except when otherwise specified) was kept throughout the test. The steady state tests were performed under atmospheric pressure at 750 °C. The reaction products were analyzed by an on-line gas chromatography (GC9790, FULI, China) and the flow rate of the tail gas was measured by a soap film flowmeter. The conversions of CH_4 and CO_2 are defined as:

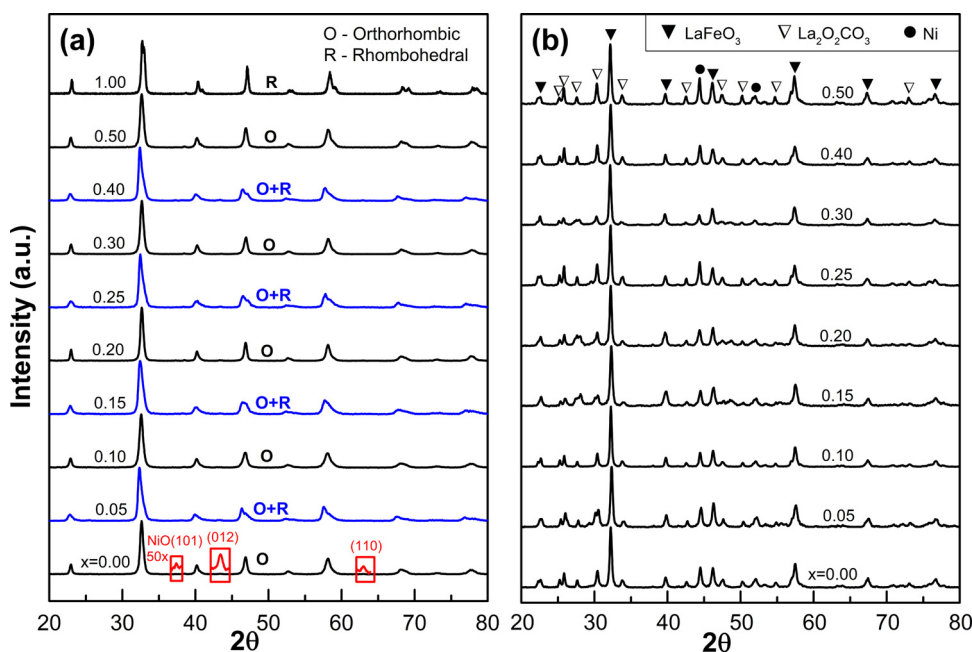


Fig. 1. XRD patterns of (a) fresh and (b) used $\text{La}(\text{Co}_x\text{Ni}_{1-x})_0.5\text{Fe}_{0.5}\text{O}_3$ samples.

$$\text{Conv CH}_4 = \frac{[\text{CH}_4]_{\text{in}} - [\text{CH}_4]_{\text{out}}}{[\text{CH}_4]_{\text{in}}} \times 100\%$$

$$\text{Conv CO}_2 = \frac{[\text{CO}_2]_{\text{in}} - [\text{CO}_2]_{\text{out}}}{[\text{CO}_2]_{\text{in}}} \times 100\%$$

where $[\text{CH}_4]_{\text{in}}$ and $[\text{CO}_2]_{\text{in}}$ refer to the molar flow rates of the introduced CH_4 and CO_2 , $[\text{CH}_4]_{\text{out}}$ and $[\text{CO}_2]_{\text{out}}$ refer to the molar flow rates of CH_4 and CO_2 in the tail gas.

3. Results

3.1. XRD

Fig. 1(a) shows the XRD patterns of fresh $\text{La}(\text{Co}_x\text{Ni}_{1-x})_0.5\text{Fe}_{0.5}\text{O}_3$ perovskite precursors. All the apparent diffraction peaks can be assigned to perovskite phases with different crystalline structures. Very weak NiO peaks can be only observed by magnifying the diffraction patterns of the Ni-containing samples (see the insets of Fig. 1). The two endmembers of the samples, LNF ($x = 0$) and LCF ($x = 1$), can be assigned to the orthorhombic (space group Pnma (62)) and rhombohedral (space group $\text{R}\bar{3}\text{c}$ (167)) crystalline structures, respectively. This analysis consists with previous reports [27–29]. By examining the XRD patterns, we can divide the intermediate compositions into two series: (A) samples with $x = 0.1, 0.2, 0.3$ and 0.5 show well defined peaks of orthorhombic crystalline structure (space group Pnma (62)), indicating that they are single-phase perovskites; (B) samples with $x = 0.05, 0.15, 0.25$ and 0.40 are characterized by asymmetric broadening or splitting of the main diffraction peaks, which cannot be assigned to a single-crystal phase structure. Detailed analysis indicates that samples in series (B) are mixed perovskites with major amount of orthorhombic phase (space group Pnma) and minor amount of rhombohedral phase (space group $\text{R}\bar{3}\text{c}$). Mixture of orthorhombic and rhombohedral phases is also observed in $\text{LaNi}_x\text{Fe}_{1-x}\text{O}_3$ and $\text{LaCo}_x\text{Fe}_{1-x}\text{O}_3$ perovskite material systems [27,30,31]. Comparing to series (A), the maxima of the main diffraction peaks of series (B) shift aggressively to lower 2θ angles, which are very close to those of orthorhombic LaFeO_3 phase (PDF#88-0641). Therefore, we deduce that the samples in series (B) separate into the Fe-rich orthorhombic and Fe-poor rhombohedral perovskites. This speculation is further proved by whole pattern fittings of the series (B) samples with 2-phase Rietveld refinement based on orthorhombic and

rhombohedral perovskite structures, which well reproduce the experimental XRD profiles. On the other hand, the XRD profiles of series (A) samples are well reproduced based on single-phase orthorhombic perovskite.

The crystalline structures and lattice parameters of all the samples abstracted by Rietveld method are summarized in Table 1. It is seen that with the increase of Co content (x), the crystalline structure of the perovskite does not change from orthorhombic to rhombohedral regularly. This should be because the $x = 0.0$ sample ($\text{LaNi}_{0.5}\text{Fe}_{0.5}\text{O}_3$) is at the margin between the orthorhombic and rhombohedral structures. It is reported that for $\text{LaFe}_x\text{Ni}_{1-x}\text{O}_3$ perovskites, samples with $x > 0.5$ show orthorhombic structure, samples with $x < 0.5$ show

Table 1

Crystalline structures and lattice parameters of fresh and used $\text{La}(\text{Co}_x\text{Ni}_{1-x})_0.5\text{Fe}_{0.5}\text{O}_3$ samples.

Samples	x	Phase	a (Å)	b (Å)	c (Å)	V/Z (Å ³)
Fresh	1.00	R	5.4850	5.4850	13.2484	57.53
	0.50	O	5.4762	7.7727	5.4863	58.38
	0.40	O	5.5331	7.8295	5.5373	59.97
		R	5.4827		13.2918	57.67
	0.30	O	5.4788	7.7703	5.4912	58.44
	0.25	O	5.5388	7.8277	5.5387	60.03
		R	5.4880		13.2917	57.78
	0.20	O	5.4723	7.7473	5.5055	58.35
	0.15	O	5.5502	7.8543	5.5455	60.46
		R	5.5114		13.3057	58.34
	0.10	O	5.4907	7.7707	5.5156	58.83
	0.05	O	5.5417	7.8486	5.5472	60.32
		R	5.4938		13.2825	57.86
	0.00	O	5.4889	7.7702	5.5195	58.85
Used	0.50	C	3.9302			60.71
	0.40	C	3.9275			60.58
	0.30	C	3.9308			60.73
	0.25	C	3.9280			60.60
	0.20	C	3.9271			60.57
	0.15	C	3.9238			60.41
	0.10	C	3.9258			60.50
	0.05	C	3.9199			60.23
	0.00	C	3.9235			60.40

Note: O: orthorhombic, space group Pnma (62).

R: rhombohedral, space group $\text{R}\bar{3}\text{c}$ (167).

C: cubic, space group $\text{Pm}\bar{3}\text{m}$ (221).

rhombohedral structure, while for the sample with $x = 0.5$, both the rhombohedral and orthorhombic phases are found [27]. Therefore, a small perturbation caused by substituting Ni with Co may drive the crystalline structure of the perovskite into orthorhombic, rhombohedral, or both.

Fig. 1(b) shows the XRD patterns of the used catalysts. Ni or Ni-Co alloy with fcc crystal structure, $\text{La}_2\text{O}_2\text{CO}_3$, and cubic perovskite LaFeO_3 (PDF#75-0541) phases are identified. The formation of $\text{La}_2\text{O}_2\text{CO}_3$ is due to the reaction of La_2O_3 with CO_2 [16]. The appearance of metallic phase and $\text{La}_2\text{O}_2\text{CO}_3$ indicates that the perovskite precursors are partially decomposed. Nevertheless, the relative intensity of the perovskite diffraction peaks is strong, indicating that the perovskite structure still survives under DRM conditions. The diffraction peaks of the perovskite in used samples can be well indexed to a cubic structure with the space group of $\text{Pm}3\text{m}$ (221), and the cell parameters refined by Rietveld method are also listed in Table 1. Under the high temperature and relatively reducing environment of DRM, most of the Ni and Co elements migrate out of the perovskite. On the contrast, Fe^{3+} cations stably exist in the lattice of LaFeO_3 , although a small amount of Co and even less amount of Ni elements may still exist in the perovskite lattice [4]. The characteristic diffraction peaks of $\text{Ni}(111)$ and $\text{Co}(111)$ are located at 44.507° (PDF#04-0850) and 44.216° (PDF#15-0806), respectively. A close examination on the $\text{Ni}(111)$ peak position in Fig. 1(b) indicates that it gradually shifts from approximate 44.49 to 44.37° as x increases from 0.0 to 0.5 , suggesting that Ni-Co alloy is formed in the intermediate composition samples which contain both Ni and Co. Formation of nano-crystalline Ni-Co alloy by reducing $\text{LaFe}_{1-x-y}\text{Ni}_x\text{Co}_y\text{O}_3$ was also observed by Wang et al. [22]. Thus, the catalysts reduced from $\text{La}(\text{Co}_x\text{Ni}_{1-x})_{0.5}\text{Fe}_{0.5}\text{O}_3$ precursors with $x = 0.05\text{--}0.50$ can be essentially considered as bimetallic Ni-Co alloys that are supported on La_2O_3 - LaFeO_3 (Ni-Co/ La_2O_3 - LaFeO_3).

Fig. 2 compares the normalized primary cell volumes (V/Z) of the perovskites in the fresh and used samples. The cell volume of used samples is much larger than that of the fresh series (A) ones and is very close to the cell volume of cubic LaFeO_3 (60.5 \AA^3 , PDF#75-0541). This is because that Ni and Co are easier to be reduced out from $\text{La}(\text{Co}_x\text{Ni}_{1-x})_{0.5}\text{Fe}_{0.5}\text{O}_3$ perovskites than Fe. Thus, LaFeO_3 turns to be the main ingredient in the remaining perovskites under DRM conditions. As discussed above, the fresh series (B) samples are mixed-perovskite with Fe-rich orthorhombic and Fe-poor rhombohedral phases. The cell volume of the series (B) Fe-rich orthorhombic phase (the composition is close to LaFeO_3) is very close to that of the used samples, while that of the Fe-poor rhombohedral phase (the composition is close to $\text{La}(\text{NiCo})\text{O}_3$, e.g. PDF#32-0296) is much smaller. This is because LaFeO_3 is more

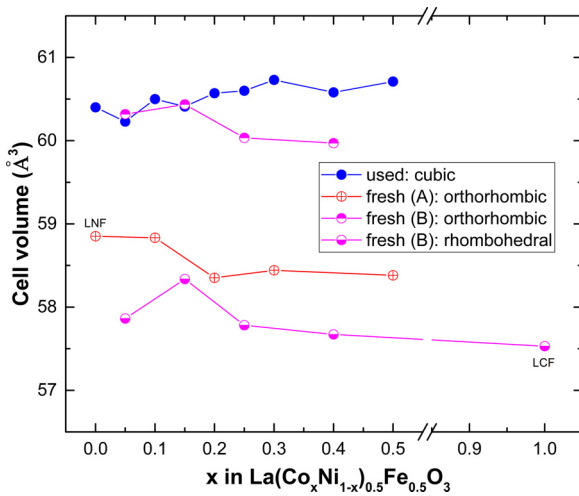


Fig. 2. Cell volume of the perovskite phases in (a) fresh and (b) used $\text{La}(\text{Co}_x\text{Ni}_{1-x})_{0.5}\text{Fe}_{0.5}\text{O}_3$ samples.

Table 2

BET surface areas (S) of fresh $\text{La}(\text{Co}_x\text{Ni}_{1-x})_{0.5}\text{Fe}_{0.5}\text{O}_3$ samples.

x	0.00	0.05	0.10	0.15	0.20	0.25	0.30	0.40	0.50	1.00
$S (\text{m}^2/\text{g})$	8.64	9.24	9.79	6.97	9.83	6.71	10.37	7.05	8.66	7.61

stable than LaCoO_3 and LaNiO_3 under reducing environment at high temperatures [32]. Therefore, the composition change in the Fe-rich phase is small after DRM test.

3.2. BET

Table 2 lists the BET surface areas of the fresh samples. The surface areas of all the samples are between $6\text{--}11 \text{ m}^2/\text{g}$. Low BET surface areas of the perovskites are commonly observed and should be attributed to the high calcination temperature during the sample preparation process [19,33,34]. The multiphase series (B) samples ($x = 0.05, 0.15, 0.25$, and 0.40) show relatively lower BET surface areas than the single-phase series (A) samples ($x = 0.10, 0.20, 0.30$, and 0.50).

3.3. TPR

Fig. 3 shows the normalized TPR profiles of fresh $\text{La}(\text{Co}_x\text{Ni}_{1-x})_{0.5}\text{Fe}_{0.5}\text{O}_3$ catalyst precursors. There are two sets of reduction peaks for each of the samples: low temperature (LT) peaks and high temperature (HT) peaks, which are located at roughly below and above 500°C , respectively. The LT and HT peaks of the single-phase samples (LCF, LNF, and series (A) samples) are well separated (Fig. 3(a), (b) and (d)), while those of the multi-phase series (B) samples overlap heavily (Fig. 3(c)). The broad temperature span of the HT peak indicates that the perovskites gradually decompose with the increase of temperature. All the perovskites decompose fully below $\sim 1000^\circ\text{C}$.

TPR signals come from the oxygen loss in the perovskite that is compensated by reducing the valence states of the metal cations. La^{3+} is hard to be reduced at the experimental conditions [35], thus the reduction peaks only correlate to the reduction of transition metal cations in the perovskite. Generally, the LT peaks reflect the reduction of active transition metals in the perovskite to intermediate valence states (e.g. Ni^{3+} to Ni^{2+} , and Co^{3+} to Co^{2+}), while the HT peaks reflect further reduction of the metal elements to their metallic form (e.g. Ni^{2+} to Ni, Co^{2+} to Co) [4,20,32,35]. For the purpose of clear appearances, we denote the reduction peak of a specific transition metal cation to its intermediate valence state by superscript α , and the reduction peak from the intermediate valence state to the metallic form by superscript β . Thus, the reduction peaks of $\text{Ni}^{3+} \rightarrow \text{Ni}^{2+}$, $\text{Co}^{3+} \rightarrow \text{Co}^{2+}$ and $\text{Fe}^{3+} \rightarrow \text{Fe}^{2+}$ are denoted as Ni^α , Co^α and Fe^α , while those of $\text{Ni}^{2+} \rightarrow \text{Ni}$, $\text{Co}^{2+} \rightarrow \text{Co}$, and $\text{Fe}^{2+} \rightarrow \text{Fe}$ are denoted as Ni^β , Co^β and Fe^β , respectively.

The TPR profile of LCF ($x = 1.0$) can be well fitted with multiple Gaussian functions as illustrated in Fig. 3(a). The fitted peak positions of Co^α , Co^β , Fe^α and Fe^β are 396.9 , 752.7 , 816.6 and 870.3°C , respectively. Both Fe^α and Fe^β appear in the HT region. This is because Fe^{3+} is stable in the octahedral crystal field of the perovskite [32]. The Fe^β peak located at the highest temperature reflects the decomposition stability of the perovskite. The area of the Co^α peak accounts for 16.9% of the total area, which is very close to the theoretic value of $1/6$ (supposing all of the Co^{3+} cations are reduced to Co^{2+}). This result confirms that Fe^{3+} cations in the perovskite can only be reduced at high temperatures, and therefore, dominate the stability of the perovskite. On the other hand, the TPR profile of LNF ($x = 0.0$) is a little complicated (Fig. 3(b)). Nevertheless, we can fit the TPR profile of LNF with multi-Gaussian functions. The fitted peak position of Ni^α is 353.9°C and the peak area is 14.3% , indicating that almost all the Ni^{3+} cations are reduced to Ni^{2+} in the LT temperature region. Comparing LCF and LNF, we see that the peak temperature of Ni^α is lower than that of Co^α ,

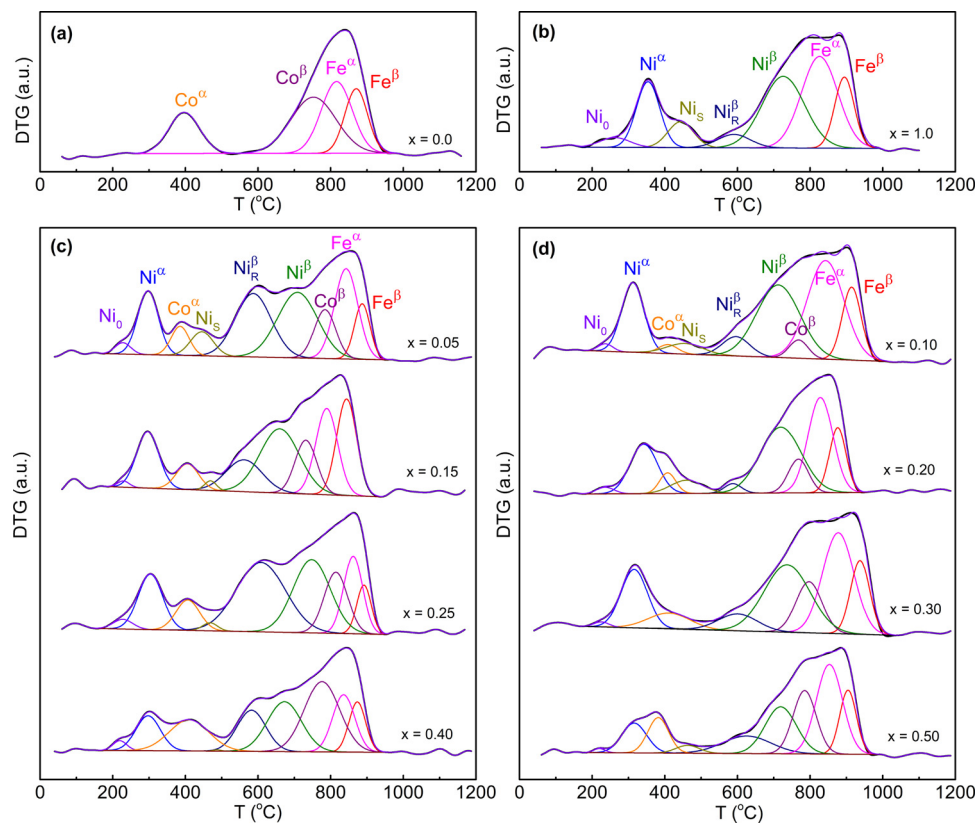


Fig. 3. TPR profiles and fitted curves of (a) LCF, (b) LNF, (c) series (B) samples ($x = 0.05, 0.15, 0.25$ and 0.40), and (d) series (A) samples ($x = 0.10, 0.20, 0.30$ and 0.50). x refers to the Co content in the $\text{La}(\text{Co}_x\text{Ni}_{1-x})_{0.5}\text{Fe}_{0.5}\text{O}_3$ precursors.

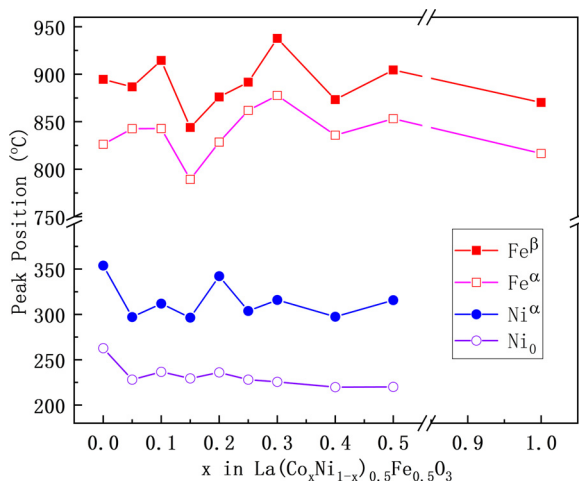


Fig. 4. TPR peak positions of Ni^α and Fe^β of all the samples derived from the fitted curves. Peak positions of Ni_0 and Fe^α are also illustrated in the figure for reference purpose.

indicating that the stability of Co^{3+} in LCF is higher than that of Ni^{3+} in LNF. Similarly, by comparing the peak positions of Fe^β (894.5 °C for LNF and 870.3 °C for LCF), we conclude that the perovskite structure of LNF is more stable than that of LCF.

Different from the case of LCF, we can see three additional peaks in the Ni-containing samples (denoted as Ni_0 , Ni_s and Ni_R^β in Fig. 3(b)-(d)). Considering NiO is detectable by XRD in the Ni-containing samples, we can assign Ni_s to the reduction of Ni^{2+} in NiO . The peak positions of Ni_s (443.7 °C) also consist with the reported reduction temperatures of NiO [6,17,19,20,36]. Ni_0 and Ni_R^β occur in all the Ni-containing samples, and locate at the left side of Ni^α and Ni^β ,

respectively. Comparing to series (A) samples (Fig. 3(d)), the peak areas of Ni_R^β are much higher in the mixed-phase series (B) samples (Fig. 3(c)). Therefore, we tend to assign Ni_R^β to the reduction of $\text{Ni}^{2+} \rightarrow \text{Ni}$ in the Fe-poor rhombohedral phase. The peak temperature of Ni_R^β is lower than that of Ni^β because Ni^{2+} cations in Fe-poor perovskite phase are readily being reduced than those in Fe-rich orthorhombic phase. We cannot resolve such rhombohedral phase in LNF and series (A) samples by XRD analyses because they exist in the samples as a minor impurity. Ni_0 occurs at the initial stage of the reduction and its area is small. Ni_0 may come from desorption of chemisorbed oxygen species, and/or similar to Ni_R^β , may originate from the reduction of $\text{Ni}^{3+} \rightarrow \text{Ni}^{2+}$ in the Fe-poor rhombohedral phase.

As expected, TPR profiles of series (A) samples (Fig. 3(d)) show similar features with that of LNF (Fig. 3(a)), and the areas of Co^α and Co^β increase with the Co content (x) respectively. Although the TPR profiles of series (B) samples can be mathematically fitted with the same set of peaks as denoted in Fig. 3(c), the physical significance of the reduction peaks is not so straightforward due to the multiple-phase nature of the samples. Different reduction peaks belonging to Fe-rich orthorhombic and Fe-poor rhombohedral crystalline structures may overlaps heavily. Fortunately, we can characterize the samples with the positions of the reduction peaks at the two ends of the TPR profiles, which should less be influenced. Fig. 4 shows the peak positions of Ni^α and Fe^β of all the samples. Peak positions of Ni_0 and Fe^α are also illustrated in the figure for reference purpose. The peak position of Ni^α (and Ni_0) reflects the feasibility of reducing Ni^{3+} , while that of Fe^β (and Fe^α) correlates with the stability of the perovskite structure. Comparing to LNF, TPR peak positions of Ni^α of all Co partially substituted samples shift to lower temperatures more or less, indicating that the incorporation of Co^{3+} in the perovskite facilitates the reduction of Ni^{3+} . On the other hand, series (A) samples show a higher average Fe^β peak temperature, which suggests that the single-phase orthorhombic perovskites are more stable than the mixed-phase ones. Obviously, the decomposition stability of

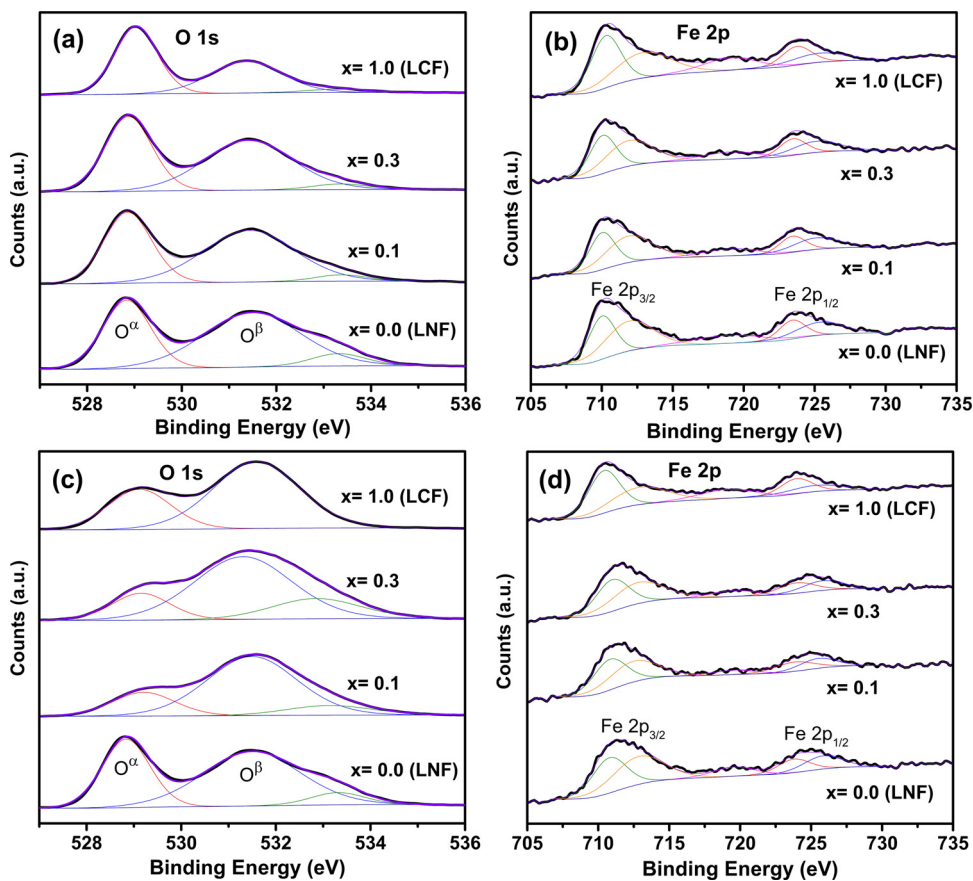


Fig. 5. XPS profiles of (a) O 1 s and (b) Fe 2p of the fresh $\text{La}(\text{Co}_x\text{Ni}_{1-x})_0.5\text{Fe}_{0.5}\text{O}_3$ samples with $x = 0.0, 0.1, 0.3$, and 1.0 ; XPS profiles of (c) O 1 s and (d) Fe 2p of the used samples with $x = 0.0, 0.1, 0.3$, and 1.0 .

the orthorhombic perovskite also depends on the Co content in the sample, which should be mainly attributed to the B-site cationic interactions between Fe and Co ions. It is worth to note that the $x = 0.1$ and 0.3 samples in series (A) have obviously higher Fe^β peak temperatures, indicating that the perovskite structures in these samples are more stable as compared to the rests.

3.4. XPS

Fig. 5 (a) and (c) show the XPS profiles of O 1s for the fresh and used samples with $x = 0.0, 0.1, 0.3$ and 1.0 . The O 1s spectra of all the samples are fitted with three peaks, which are labeled as O_α (~ 528.9 eV), O_β (~ 531.4 eV) and O_γ (~ 533.3 eV), respectively. According to previous literatures, O_α (with the lowest binding energy) can be assigned to lattice oxygen, while O_β and O_γ can be assigned to surface oxygen species, such as hydroxyl and/or carbonate species (~ 531.4 eV), and adsorbed water (~ 533.3 eV), respectively [37–41]. The $\text{O}_\beta/\text{O}_\alpha$ ratios of the used samples are obviously larger than those of the fresh ones, suggesting that there are more surface adsorbed oxygen species, which may correlate to the undercoordinated B-site cations and oxygen vacancies generated in the perovskites under DRM conditions [17,42]. It should be mentioned that both the perovskite and $\text{La}_2\text{O}_2\text{CO}_3$ phases are clearly identified in the used samples (See Fig. 1 (b)). Thus, in addition to the oxygen species related to the perovskite, oxygen species in $\text{La}_2\text{O}_2\text{CO}_3$ should also contribute to the O 1s spectra of the used samples [38]. Formation of $\text{La}_2\text{O}_2\text{CO}_3$ is known to have a promotion effect on the catalytic activity and coking resistance of Ni-Co bimetallic catalysts [5].

The XPS profiles of Fe 2p for the fresh and used samples are curve-fitted and shown in Fig. 5 (b) and (d). The Fe 2p_{3/2} and 2p_{1/2} features can be well fitted with two sets of peaks, which should be ascribed to

Fe^{3+} [39,43,44]. The peak located at about 719 eV is assigned to the satellite peak of $\text{Fe} 2p_{3/2}$ [44]. It is noticed that the shapes and positions of the Fe 2p peaks are very similar before and after DRM tests, while no peaks belonging to Fe^0 can be observed in the used samples, suggesting that the Fe^{3+} cations in the perovskite are stable. This observation consists with our XRD analyses, which indicates that LaFeO_3 perovskite stably exists and becomes the main ingredient in the used catalysts.

3.5. Catalytic activity

Fig. 6 (a) and (b) shows conversions of CH_4 and CO_2 over reduced $\text{La}(\text{Co}_x\text{Ni}_{1-x})_0.5\text{Fe}_{0.5}\text{O}_3$ catalysts as a function of reaction time. The catalytic activity strongly depends on the substitution degree of Co (x). LNF has been proved to be a good catalyst precursor for DRM reactions and has been well studied [4,14]. In the present case, conversions of CH_4 and CO_2 over LNF reach 46% and 64% after 5 h DRM test, respectively. On the other hand, LCF shows a very poor catalytic performance because Co is not so active as compared to Ni for DRM reactions [1,16]. Nevertheless, it is interesting to see that the catalytic activity increases obviously by substituting a proper amount of Co in $\text{La}(\text{Co}_x\text{Ni}_{1-x})_0.5\text{Fe}_{0.5}\text{O}_3$ ($x = 0.05 – 0.4$). It is also seen that catalysts with higher CH_4 and CO_2 conversions (e.g., samples with $x = 0.1$ and 0.3) are stable over 5 h test, while those with lower CH_4 and CO_2 conversions (e.g., samples with $x = 0.0, 0.5$, and 1.0) require more activation time to reach equilibrium during DRM reactions.

Fig. 6 (c) shows the H_2/CO ratios in the tail gas for different samples. Assuming no carbon formation occurs, the theoretical equilibrium H_2/CO ratio under atmospheric pressure at 750°C and $\text{CH}_4/\text{CO}_2 = 1$ is approximate 0.92 [2]. However, the actual value is affected by side reactions, such as the RWGS reaction, CH_4 decomposition reaction, and

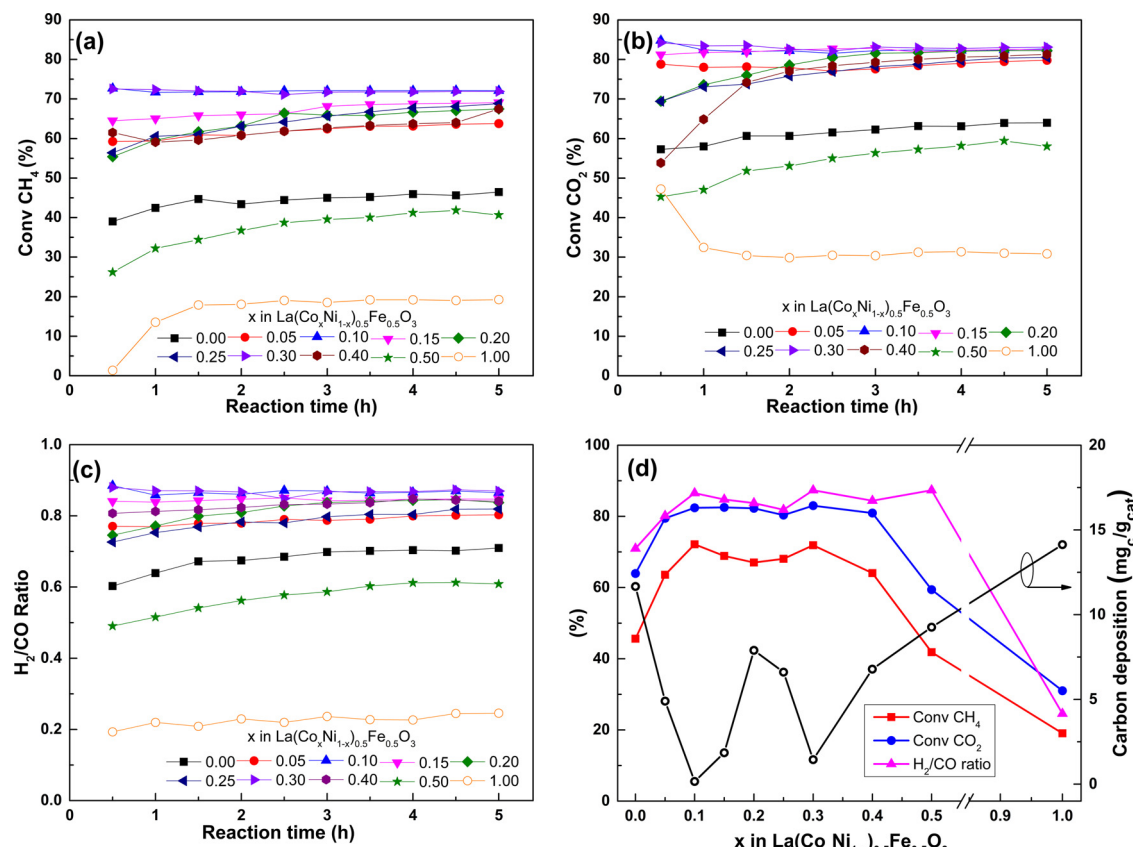


Fig. 6. (a) CH₄ conversion, (b) CO₂ conversion, and (c) H₂/CO ratio as a function of reaction time during the DRM reactions over La(Co_xNi_{1-x})_{0.5}Fe_{0.5}O₃ with different x values. (d) Changes of CH₄, CO₂ conversions, H₂/CO ratio, and carbon deposition with x. The data reported in Fig. 6(d) are those collected at the reaction time of 5 h.

the Boudouard reaction. The H₂/CO ratios of all samples are less than 0.9, and the CH₄ conversions are lower than the corresponding CO₂ conversions, indicating that the RWGS reaction dominates the side reactions.

Fig. 6 (d) summarizes the conversions of CH₄, CO₂ and the H₂/CO ratios, which are taken at the reaction time of 5 h for different samples. Maximal catalytic activities are observed at x = 0.1 and 0.3, where the CH₄ conversions are above 70%. The CO₂ conversions also show the same changing trend, and reach above 80% at x = 0.1 and 0.3. As a comparison, conversions of CH₄ and CO₂ over LNF is only ~46% and ~64%, respectively. The results indicate that substituting a proper amount of Ni by Co in La(Co_xNi_{1-x})_{0.5}Fe_{0.5}O₃ has a significant effect on enhancing the catalytic activity for DRM reactions.

In order to evaluate the long-term performance of the catalysts, we extend the DRM test time of the x = 0.1 and 0.3 samples to 30 h (see Fig. 7). Both the conversions of CH₄ and CO₂ are stable, and the amount of deposited carbon are negligible (below 2 mg_C/g_{cat}). Assuming no carbon formation occurs, the theoretical thermodynamic equilibrium conversions of CH₄ and CO₂ for DRM reaction under atmospheric pressure at 750 °C and CH₄/CO₂ = 1 are reported to be approximate 83% and 90%, respectively [2]. Table 3 compares the performance of our catalysts to those published in recent literatures under similar experimental conditions. The performance of the catalysts reported in this work is competitive even the conversions of CH₄ and CO₂ are apparently lower than the equilibrium conversions. Higher catalytic activity can be expected by increasing the specific surface area of the catalysts and/or increasing the dispersion of the metallic phase.

The x = 0.1 sample (La(Co_{0.1}Ni_{0.9})_{0.5}Fe_{0.5}O₃) was also tested under a higher GHSV of 3.6 × 10⁴ mL g⁻¹ h⁻¹, and the results are shown in Fig. 8. The CH₄ and CO₂ conversions without catalyst dilution are ~55.5% and 70.5%, respectively. The CH₄ and CO₂ conversions further

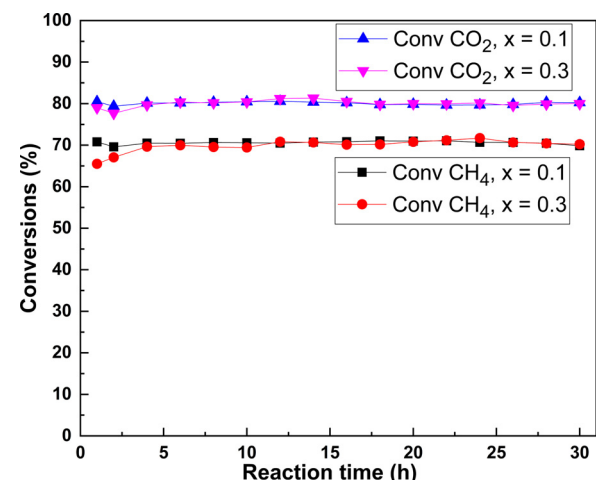


Fig. 7. Conversions of CH₄ and CO₂ for 30-hour DRM reactions over La(Co_xNi_{1-x})_{0.5}Fe_{0.5}O₃ with x = 0.1 and 0.3.

increase to ~63.5% and 80.0% by diluting the catalyst with quartz sand. The increased activity of the diluted catalyst should be largely attributed to the improvement of heat transfer in the fixed bed reactor [55,56]. For both cases, the amount of deposited carbon after 30-h tests are negligible (below 3 mg_C/g_{cat}) as determined by TPO analysis.

3.6. Carbon deposition

In addition to the catalytic activity, reducing the amount of carbon deposition during the high temperature process of DRM is also very

Table 3

Examples of the catalytic performance of Ni and Ni-Co based catalysts for DRM.

Precursor or Catalyst/support	Catalyst weight (mg)	Inlet gas composition, vol.%	Gas feeding (ml/min)	Total GHSV (mLg ⁻¹ h ⁻¹)	Reaction temperature (C°)	CH ₄ Conv. (%)	CO ₂ Conv. (%)	Test time (h)	Year/Ref.
La(Co _{0.1} Ni _{0.9}) _{0.5} Fe _{0.5} O ₃	300	50%CH ₄ , 50%CO ₂	60	12,000	750	70	80	30	This work
La _{0.4} Ce _{0.6} Ni _{0.5} Fe _{0.5} O ₃	300	50%CH ₄ , 50%CO ₂	60	12,000	750	62	72	25	2018 [46]
Ni-Co/Ca ₁₀ (PO ₄) ₆ (OH) ₂	340	20%CH ₄ , 20%CO ₂ , 60% N ₂	90	(~ 16,000)	750	73	79	160	2018 [45]
Ni/h-BN nanosheet	120	50%CH ₄ , 50%CO ₂		15,000	750	88	97	120	2018 [47]
4%Ni-1%Co/SBA-15	100	33%CH ₄ , 33%CO ₂ , 33%Ar	60	36,000	750	73	89	4	2018 [48]
LaNiO ₃ /CeSiO ₂		50%CH ₄ , 50%CO ₂	100		800	58	73	24	2018 [49]
Ni9Co1/SBA-15	50	50%CH ₄ , 50%CO ₂	60	72,000	800	90.4	94.9	50	2018 [50]
Ni/BN@mSiO ₂	120	50%CH ₄ , 50%CO ₂		15,000	750	83	96	100	2017 [51]
7%Ni-3%Co phyllosilicates/SiO ₂	30	33%CH ₄ , 33%CO ₂ , 33%He	30	60,000	750	84	88	100	2017 [52]
Ni/Al ₂ O ₃ -CeO ₂	100	50%CH ₄ , 50%CO ₂	40	24,000	750	88	94	10	2017 [53]
ALD Ni/ γ -Al ₂ O ₃	0.64(Ni)	20%CH ₄ , 20%CO ₂ , 60%Ar	100	9,375,000	750	71		250	2017 [54]
Ni/SiO ₂	100	45%CH ₄ , 45%CO ₂ , 10%N ₂	20	12,000	800	37	62	100	2017 [6]
Ni/Al ₂ O ₃						40	50	20	
Ni/MgO						40	55	20	

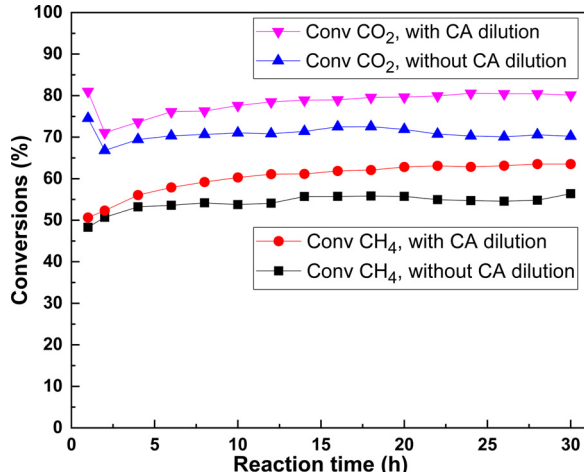


Fig. 8. Conversions of CH₄ and CO₂ for 30-h DRM reactions over La(Co_{0.1}Ni_{0.9})_{0.5}Fe_{0.5}O₃ at 750 °C and GHSV = 3.6 × 10⁴ mLg⁻¹ h⁻¹. The GHSV was realized by reducing the catalyst loading to 100 mg while maintaining the composition and total flow rate of the inlet gas at 60 sccm. Catalytic performances with/without catalyst dilution are compared.

important [1,7,33,45]. The amounts of deposited carbon in the used catalysts with different Co contents are also shown in Fig. 6(d). The values in all the samples are below 15 mg_C/g_{cat} after 5 h DRM test. The overall slow carbon formation rate should be attributed to the stable perovskite phase in the catalysts, which enhances metal-support interaction and promotes the removal of deposited carbon species [4,21]. Even so, we can see that the carbon formation rates of all the Co partial substituted samples ($x = 0.05 - 0.5$) are lower than that of LNF. It is interesting to note that the carbon formation rate is roughly inversely proportional to the CH₄ conversion: the higher the CH₄ conversion, the lower the carbon formation rate. Especially, the $x = 0.10$ and 0.30 samples which show maximal catalytic activities also present minimal carbon formation rates. Even after 30-h tests, the amount of deposited carbon for these two samples are still very low (0.8 mg_C/g_{cat} for the $x = 0.10$ sample, and 1.5 mg_C/g_{cat} for the $x = 0.30$ sample). Thus, a proper amount of Co substitution in LNF not only enhances the catalytic activity, but also obviously suppresses carbon deposition in the catalysts.

Fig. 9 shows the typical SEM (left column) and TEM (middle column) images, and metallic size distributions (right column) of the used samples with $x = 0.0, 0.1, 0.2, 0.3$ and 0.4. All the samples show

similar porous morphology, and no filamentous carbon can be observed. In a previous work, we have demonstrated that the catalyst reduced from LaNi_{0.5}Fe_{0.5}O₃ precursor presents high coking resistance [4], which agrees well with the present work. The TEM images show that metallic Ni or Ni-Co particles are homogeneously distributed on the support. The metallic particle size distributions of all the samples are similar, and the average particle size is about 18 nm. It is accepted that the coking resistance of Ni based catalysts depends on the metallic particle size [1]. Kim et al. [57] studied DRM reactions over Ni/Al₂O₃ catalysts and found that formation of filamentous carbon happens on the catalysts when the average particle size of Ni is larger than approximate 7 nm. In the present work, it is hard to find any filamentous carbon though the average metallic particle size is ~18 nm. A similar observation was also reported by Sutthiumporn et al. [37]. They observed that the amount of deposited carbon for La_{0.8}Sr_{0.2}Ni_{0.8}Fe_{0.2}O₃ catalyst is negligible after 10-h DRM test at 700 °C, even the metallic particle size is ~20 nm. The high coking resistance should be attributed to the strong metal-support interactoin. Moreover, oxygen affinity of Co in the metallic particles and the active oxygen species in the perovskite should also be helpful for removing the deposited carbon species.

Although no filamentous carbon can be observed, we still find very few nanosheet-like carbon species by chance. Fig. 10 shows a high resolution TEM image of the $x = 0.10$ sample, which presents the lowest carbon deposition rate (see Fig. 6(d)). The FFT patterns (insets of Fig. 10) corresponding to the support and the metallic particle can be well indexed to cubic LaFeO₃ and cubic Ni structures, respectively. Thus, it is seen that a Ni-Co particle of ~18 nm in diameter is well embedded on the LaFeO₃ perovskite matrix, indicating a strong metal-support interaction. It is noticed that a collection of fringes continuously spreads from about the center of the Ni-Co particle to the LaFeO₃ matrix, which should be assigned to the deposited carbon species. The spacing between the fringes of carbon species is ~0.345 nm, which is approximate to the interlayer spacing in a graphite lattice ($d(002) = 3.3555 \text{ \AA}$, PDF#65-6212), indicating no C–C bond is formed (at least along the direction acrossing the fringes). Thus, the deposited carbon species are not stable and can be easily removed by oxygen species adsorbed either on the metallic particle or on the perovskite matrix.

4. Discussion

4.1. Effect of Ni/Co ratio

The results in Section 3 suggest that the activities of the catalysts

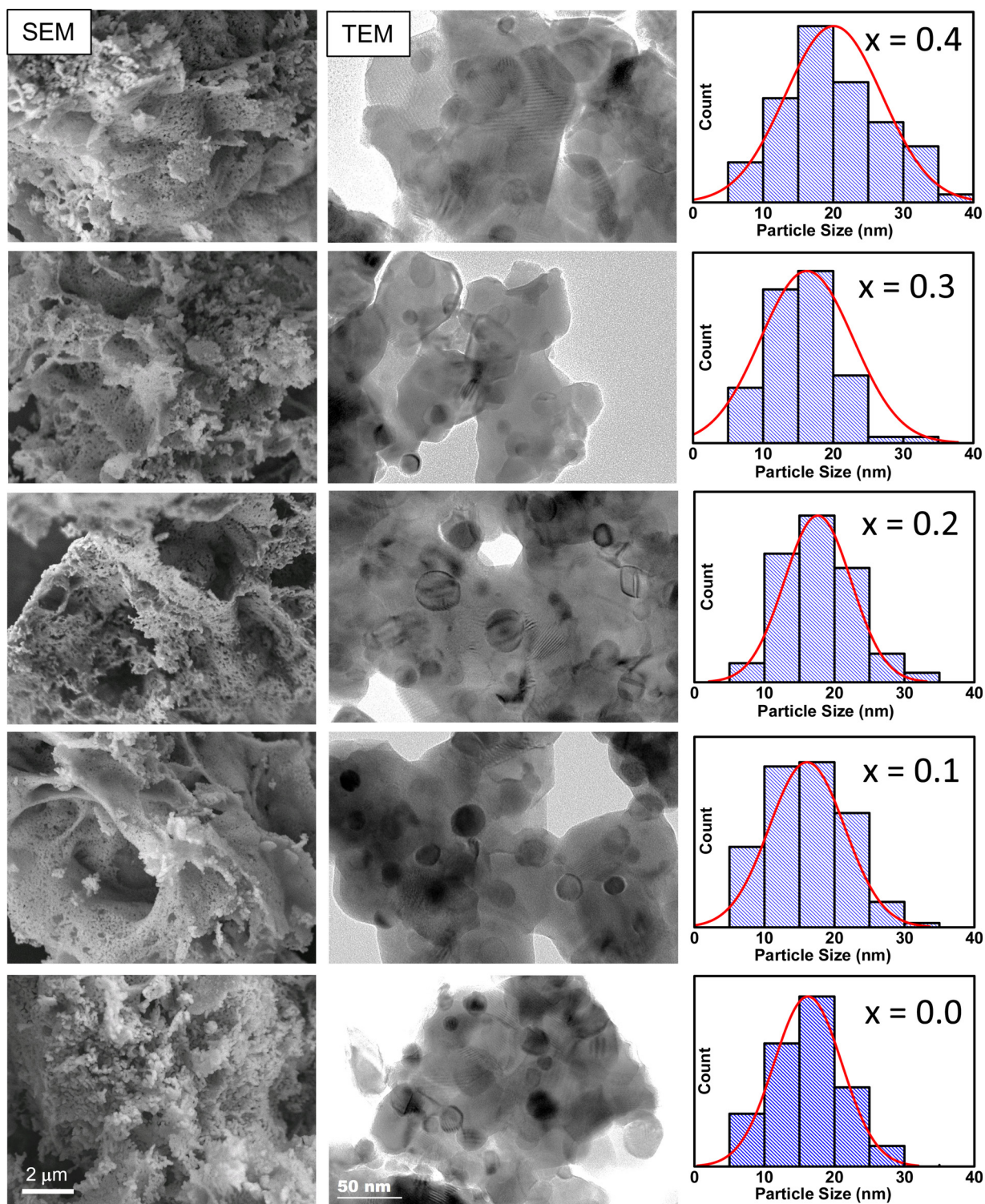


Fig. 9. Typical SEM (left column) and TEM (middle column) images, and metallic size distributions (right column) of the used $\text{La}(\text{Co}_x\text{Ni}_{1-x})_0.5\text{Fe}_0.5\text{O}_3$ samples with $x = 0.0, 0.1, 0.2, 0.3$ and 0.4 . The metallic particle size distributions are statistically analyzed over about 150 particles for each sample.

reduced from $\text{La}(\text{Co}_x\text{Ni}_{1-x})_0.5\text{Fe}_0.5\text{O}_3$ precursors strongly depend on the Co content. In the Ni-Co/ $\text{LaFeO}_3\text{-La}_2\text{O}_3$ catalysts, metallic Ni-Co particles should be the main component for the activation of CH_4 . Comparing to LNF, the overall enhanced conversions of CH_4 over the catalysts with $x = 0.05 – 0.40$ should be mainly attributed to the formation of Ni-Co bimetallic particles. It is reported that the Co/Ni ratio is crucial for the activity in Ni-Co bimetallic catalysts: a small Co content is enough to enhance the activity, but a too high Co content will suppress

the activity to lower than that of Ni monometallic catalysts [1]. Our results shown in Fig. 6(d) agree well with the reported observations. The promotion of Co on the activity of the Ni-Co bimetallic catalysts is mainly originated from the strong affinity of Co to oxygen species [1,58].

It is desirable to evaluate the catalytic activities of the active metallic components in terms of turnover frequencies (TOFs). However, changes of CH_4 and CO_2 conversions are small, especially in the Co

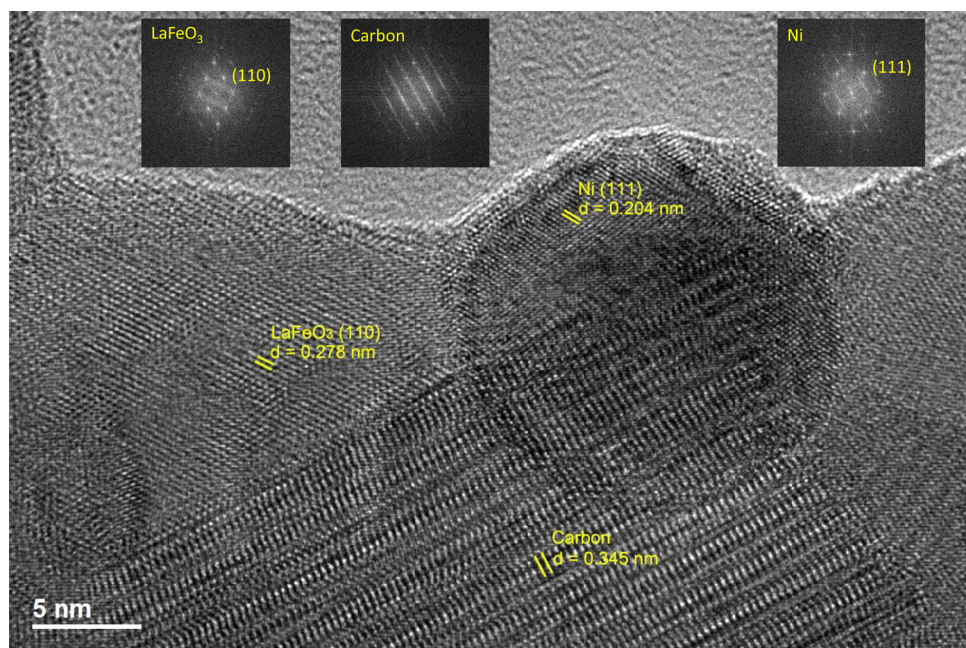


Fig. 10. High resolution TEM image of used $\text{La}(\text{Co}_{0.1}\text{Ni}_{0.9})_{0.5}\text{Fe}_{0.5}\text{O}_3$ sample. The insets are selective area FFT patterns.

content range of $x = 0.05 - 0.40$. Accurate measurements of the metallic surface area and dispersion are problematic due to the influences of the perovskite phase [19,59]. Moreover, as will be discussed below, the perovskite phase in the catalysts may also activate conversions of both CH_4 and CO_2 , which makes it unreasonable to attribute all the turnover events to the active metallic components.

4.2. Effect of perovskite structure

It is more interesting to note that catalysts ($x = 0.10$ and 0.30) with the most stable orthorhombic perovskite structure (Fig. 4) appear to have the highest catalytic activity and coking resistance (Fig. 6(d)). This observation strongly suggests that the crystalline structure of the perovskite plays an important role in the performance of the catalysts during DRM reactions. Moreover, the single-phase series (A) samples show relatively higher BET surface areas than the multiphase series (B) samples (Table 2). For examples, the surface areas of the $x = 0.1$, 0.2 and 0.3 samples (series (A)) are $\sim 10 \text{ m}^2/\text{g}$, while those of the $x = 0.15$, 0.25 and 0.40 samples (series (B)) are $\sim 7 \text{ m}^2/\text{g}$. The relatively high initial surface areas together with the high decomposition stability of the $x = 0.10$ and 0.30 samples ensure that there are more perovskite components remaining in the catalysts after H_2 reduction and/or during DRM reactions. On the other hand, although the surface area of the $x = 0.2$ sample is equivalently high, but its decomposition stability is low. As a result, the amount of remaining perovskite in the $x = 0.20$ catalyst should be small.

It is known that the metal-support interaction may affect the size distribution of metallic particles, and in turn affects the catalytic activity and coking resistance [60]. However, in the present study, all the samples show similar average metallic particle size of $\sim 18 \text{ nm}$ (Fig. 9). Thus, we cannot attribute the improved performance of the $x = 0.10$ and 0.30 samples to the particle size effect.

For DRM reactions, it is widely accepted that the metal-support synergistic effect may strongly affect the activity and coking resistance of the catalysts. Such a synergistic effect describes that CH_4 is activated on the metal while CO_2 is activated on the oxide support [2]. The perovskite support is featured by oxygen vacancies and active oxygen species, especially under the high temperature and relatively reducing atmosphere of DRM [30,61]. The oxygen vacancies provide active sites for the dissociation of CO_2 , while the active oxygen species promote

both the partial oxidation of CH_4 and the removal of deposited carbon species [14].

Interestingly, the decomposing stability of the perovskites (reflected by the Fe^β TRP peak position in Fig. 4) is enhanced obviously at some specific Co contents ($x = 0.10$ and 0.30). It is seen in Fig. 2 that the cell volume of the LaFeO_3 phase in the used catalysts shows a slightly expanding trend with x , indicating that the composition of the perovskites is different. Considering that our DRM tests were performed at 750°C , where the perovskite precursors were partially reduced, there should be some residual amount of Co (and even Ni) remains in the LaFeO_3 lattice in the used catalysts. The multivalence feature of Co may well compensate the valence change of the transition metal cations induced by the loss of oxygen under reducing atmosphere. Moreover, even with the same valence state, Co ions may present multiple spin states in a perovskite, such as low spin (LS: $t_{2g}^6e_g^0$), intermediate spin (IS: $t_{2g}^5e_g^1$), and high spin (HS: $t_{2g}^4e_g^2$) states of Co^{3+} ions [62]. Changes in the valence and/or spin state of a Co ion will also induce changes in the ionic radius, as well as the electronic structure of the perovskite. The multiple valence and spin states features of Co cations provide extra freedom for the crystalline structure of a perovskite. Thus, the interplay between the different B-site elements (e.g. Co and Fe) may affect the stability and catalytic properties of a perovskite.

Thus, we conclude that crystalline structure of the perovskite precursors affects its stability, and in turn, dominates the amount of remaining perovskite in the catalysts under DRM conditions. The remaining perovskite component promotes both the partial oxidation of CH_4 and the removal of deposited carbon species. This also explains why the samples with $x = 0.10$ and 0.30 present the highest catalytic activity and coking resistance.

5. Conclusions

Bimetallic Ni-Co catalysts supported on $\text{La}_2\text{O}_3\text{-LaFeO}_3$ for DRM reactions were prepared by reducing $\text{La}(\text{Co}_x\text{Ni}_{1-x})_{0.5}\text{Fe}_{0.5}\text{O}_3$ perovskite precursors. The catalytic activity and coking resistance are obviously enhanced by substituting a proper amount of Co ($x = 0.05 - 0.40$), which should be essentially attributed to the synergistic effect between Ni and Co.

It is also found that the crystalline structure of the perovskite precursors depends on the Co content. LNF and LCF present orthorhombic

and rhombohedral crystalline structures respectively, while the intermediate compositions adopt either orthorhombic or mixed orthorhombic-rhombohedral structure. Catalysts reduced from orthorhombic perovskite precursors with $x = 0.10$ and 0.30 , which have obviously higher structural stability, show maximal catalytic activity and coking resistance.

Our results suggest that a stable perovskite is preferred for DRM reactions. The promotion effect of the perovskite support is probably related to the active oxygen species in the perovskites, which promote both the DRM reactions and the removal of deposited carbon species.

Acknowledgement

This work is supported by the National Natural Science Foundation of China (Grant No.: 21872129 and No.: 21427804).

References

- [1] Z. Bian, S. Das, M.H. Wai, P. Hongmanorom, S. Kawi, A review on bimetallic nickel-based catalysts for CO₂ reforming of methane, *Chemphyschem* 18 (2017) 3117–3134.
- [2] D. Pakhare, J. Spivey, A review of dry (CO₂) reforming of methane over noble metal catalysts, *Chem. Soc. Rev.* 43 (2014) 7813–7837.
- [3] Y. Vafaeian, M. Haghghi, S. Aghamohammadi, Ultrasound assisted dispersion of different amount of Ni over ZSM-5 used as nanostructured catalyst for hydrogen production via CO₂ reforming of methane, *Energy Convers. Manage.* 76 (2013) 1093–1103.
- [4] X. Song, X.L. Dong, S.L. Yin, M. Wang, M. Li, H.Q. Wang, Effects of Fe partial substitution of La₂NiO₄/LaNiO₃ catalyst precursors prepared by wet impregnation method for the dry reforming of methane, *Appl. Catal. a-Gen.* 526 (2016) 132–138.
- [5] A. Tsoukalou, Q. Imtiaz, S.M. Kim, P.M. Abdala, S. Yoon, C.R. Müller, Dry-reforming of methane over bimetallic Ni–M/La 2 O 3 (M = Co, Fe): the effect of the rate of La 2 O 2 CO 3 formation and phase stability on the catalytic activity and stability, *J. Catal.* 343 (2016) 208–214.
- [6] J.W. Han, J.S. Park, M.S. Choi, H. Lee, Uncoupling the size and support effects of Ni catalysts for dry reforming of methane, *Appl. Catal. B* 203 (2017) 625–632.
- [7] N.A.K. Aramouni, J.G. Touma, B. Abu Tarboush, J. Zeaiter, M.N. Ahmad, Catalyst design for dry reforming of methane: analysis review, *Renew. Sustain. Energy Rev.* 82 (2018) 2570–2585.
- [8] G. Wu, S. Li, C. Zhang, T. Wang, J. Gong, Glycerol steam reforming over perovskite-derived nickel-based catalysts, *Appl. Catal. B* 144 (2014) 277–285.
- [9] Z. Wang, X.M. Cao, J. Zhu, P. Hu, Activity and coke formation of nickel and nickel carbide in dry reforming: a deactivation scheme from density functional theory, *J. Catal.* 311 (2014) 469–480.
- [10] B. AlSabban, L. Falivene, S.M. Kozlov, A. Aguilar-Tapia, S. Ould-Chikh, J.-L. Hazemann, L. Cavallo, J.-M. Basset, K. Takanabe, In-operando elucidation of bimetallic CoNi nanoparticles during high-temperature CH₄ /CO₂ reaction, *Appl. Catal. B* 213 (2017) 177–189.
- [11] H. Arbag, S. Yasyerli, N. Yasyerli, G. Dogu, T. Dogu, Enhancement of catalytic performance of Ni based mesoporous alumina by Co incorporation in conversion of biogas to synthesis gas, *Appl. Catal. B* 198 (2016) 254–265.
- [12] J. Zhang, H. Wang, A. Dalai, Development of stable bimetallic catalysts for carbon dioxide reforming of methane, *J. Catal.* 249 (2007) 300–310.
- [13] X. Fan, Z. Liu, Y.-A. Zhu, G. Tong, J. Zhang, C. Engelbrekt, J. Ulstrup, K. Zhu, X. Zhou, Tuning the composition of metastable Co_x Ni_y Mg_{100-x-y}(OH)₁₀ (OCH₃) nanoplates for optimizing robust methane dry reforming catalyst, *J. Catal.* 330 (2015) 106–119.
- [14] Q. Yang, G. Liu, Y. Liu, Perovskite-type oxides as the catalyst precursors for preparing supported metallic nanocatalysts: a review, *Ind. Eng. Chem. Res.* 57 (2017) 1–17.
- [15] F. Liu, Y. Qu, Y. Yue, G. Liu, Y. Liu, Nano bimetallic alloy of Ni–Co obtained from LaCoxNi_{1-x}O₃ and its catalytic performance for steam reforming of ethanol, *RSC Adv.* 5 (2015) 16837–16846.
- [16] G. Valderrama, A. Kiennemann, M.R. Goldwasser, Dry reforming of CH₄ over solid solutions of LaNi_{1-x}CoxO₃, *Catal. Today* 133–135 (2008) 142–148.
- [17] M. Wang, T. Zhao, X. Dong, M. Li, H. Wang, Effects of Ce substitution at the A-site of LaNi_{0.5}F_{0.5}O₃ perovskite on the enhanced catalytic activity for dry reforming of methane, *Appl. Catal. B* 224 (2018) 214–221.
- [18] D. Burnat, R. Kontic, L. Holzer, P. Steiger, D. Ferri, A. Heel, Smart material concept: reversible microstructural self-regeneration for catalytic applications, *J. Mater. Chem. A Mater. Energy Sustain.* 4 (2016) 11939–11948.
- [19] P. Steiger, R. Delmelle, D. Foppiano, L. Holzer, A. Heel, M. Nachtegaal, O. Krocher, D. Ferri, Structural reversibility and nickel particle stability in lanthanum Iron nickel perovskite-type catalysts, *ChemSusChem* 10 (2017) 2505–2517.
- [20] R. Pérenigüez, V.M. González-delaCruz, A. Caballero, J.P. Holgado, LaNiO₃ as a precursor of Ni/La₂O₃ for CO₂ reforming of CH₄: Effect of the presence of an amorphous NiO phase, *Appl. Catal. B* 123–124 (2012) 324–332.
- [21] H. Arandian, J. Li, L. Ma, S.M. Hashemnejad, M.Z. Mirzaei, J. Chen, H. Chang, C. Liu, C. Wang, L. Chen, Methane reforming to syngas over LaNi_xFe_{1-x}O₃ ($0 \leq x \leq 1$) mixed-oxide perovskites in the presence of CO₂ and O₂, *J. Ind. Eng. Chem.* 18 (2012) 2103–2114.
- [22] Z. Wang, C. Wang, S. Chen, Y. Liu, Co–Ni bimetal catalyst supported on perovskite-type oxide for steam reforming of ethanol to produce hydrogen, *Int. J. Hydrogen Energy* 39 (2014) 5644–5652.
- [23] G. Pecchi, C.M. Campos, M.G. Jiliberto, E.J. Delgado, J.L.G. Fierro, Effect of additive Ag on the physicochemical and catalytic properties of LaMn_{0.9}Co_{0.1}O_{3.5} perovskite, *Appl. Catal. A Gen.* 371 (2009) 78–84.
- [24] L. Bedel, A.C. Roger, C. Estournes, A. Kiennemann, Co₀ from partial reduction of La (Co,Fe)O₃ perovskites for Fischer–Tropsch synthesis, *Catal. Today* 85 (2003) 207–218.
- [25] E. Grabowska, Selected perovskite oxides: characterization, preparation and photocatalytic properties—a review, *Appl. Catal. B* 186 (2016) 97–126.
- [26] J. Shi, L. Guo, AB₃-based photocatalysts for water splitting, *Prog. Nat. Sci.* 22 (2012) 592–615.
- [27] H. Falcon, A.E. Goeta, G. Punte, R.E. Carbonio, Crystal structure refinement and stability of LaFeNi_{1-x}O₃ solid solutions, *J. Solid State Chem.* 133 (1997) 379–385.
- [28] N.A. Merino, B.P. Barbero, P. Ruiz, L.E. Cadús, Synthesis, characterisation, catalytic activity and structural stability of LaCo_{1-y}Fe_yO₃ ± λ perovskite catalysts for combustion of ethanol and propane, *J. Catal.* 240 (2006) 245–257.
- [29] D.V. Karpinsky, I.O. Troyanchuk, K. Bärner, H. Szyszczak, M. Tovar, Crystal structure and magnetic ordering of the LaCo_{1-x}Fe_xO₃ system, *J. Phys. Condens. Matter* 17 (2005) 7219–7226.
- [30] M. Pishahang, E. Bakken, S. Stolen, C.I. Thomas, P.I. Dahl, Oxygen non-stoichiometry, redox thermodynamics, and structure of LaFe_{1-x}Co_xO₃₋₈, *Ionicics* 19 (2012) 869–878.
- [31] N. Escalona, S. Fuentelba, G. Pecchi, Fischer–Tropsch synthesis over LaFe_{1-x}CoxO₃ perovskites from a simulated biosyngas feed, *Appl. Catal. A Gen.* 381 (2010) 253–260.
- [32] T. Nakamura, G. Petzow, L.J. Gauckler, Stability of the perovskite phase LaBO₃ (B = V, Cr, Mn, Fe, Co, Ni) in reducing atmosphere I. Experimental results, *Mater. Res. Bull.* 14 (1979) 649–659.
- [33] R.C. Rabelo-Neto, H.B.E. Sales, C.V.M. Inocencio, E. Varga, A. Oszko, A. Erdohelyi, F.B. Noronha, L.V. Mattos, CO₂ reforming of methane over supported LaNiO₃ perovskite-type oxides, *Appl. Catal. B* 221 (2018) 349–361.
- [34] E. le Saché, L. Pastor-Pérez, D. Watson, A. Sepúlveda-Escribano, T.R. Reina, Ni stabilised on inorganic complex structures: superior catalysts for chemical CO₂ recycling via dry reforming of methane, *Appl. Catal. B* 236 (2018) 458–465.
- [35] M. Ao, G.H. Pham, V. Sage, V. Pareek, Structure and activity of strontium substituted LaCoO₃ perovskite catalysts for syngas conversion, *J. Mol. Catal. A Chem.* 416 (2016) 96–104.
- [36] T. Guo, X. Dong, M.M. Shirolkar, X. Song, M. Wang, L. Zhang, M. Li, H. Wang, Effects of cobalt addition on the catalytic activity of the Ni-YSZ anode functional layer and the electrochemical performance of solid oxide fuel cells, *ACS Appl. Mater. Interfaces* 6 (2014) 16131–16139.
- [37] K. Sutthiumporn, T. Maneerung, Y. Kathiraser, S. Kawi, CO₂ dry-reforming of methane over La_{0.85}Pr_{0.2}Ni_{0.8}Mn_{0.2}O₃ perovskite (M = Bi, Co, Cr, Cu, Fe): roles of lattice oxygen on C–H activation and carbon suppression, *Int. J. Hydrogen Energy* 37 (2012) 11195–11207.
- [38] P.A.W. van der Heide, Systematic x-ray photoelectron spectroscopic study of La_{1-x}Sr_x-based perovskite-type oxides, *Surf. Interface Anal.* 33 (2002) 414–425.
- [39] Y. Zheng, K. Li, H. Wang, D. Tian, Y. Wang, X. Zhu, Y. Wei, M. Zheng, Y. Luo, Designed oxygen carriers from macroporous LaFeO₃ supported CeO₂ for chemical-looping reforming of methane, *Appl. Catal. B* 202 (2017) 51–63.
- [40] N.A. Merino, B.P. Barbero, P. Eloy, L.E. Cadús, La_{1-x}CaxCoO₃ perovskite-type oxides: identification of the surface oxygen species by XPS, *Appl. Surf. Sci.* 253 (2006) 1489–1493.
- [41] O.P. Taran, A.B. Ayusheev, O.L. Ogorodnikova, I.P. Prosvirin, L.A. Isupova, V.N. Parmon, Perovskite-like catalysts LaBO₃ (B = Cu, Fe, Mn, Co, Ni) for wet peroxide oxidation of phenol, *Appl. Catal. B* 180 (2016) 86–93.
- [42] J. Suntivich, H.A. Gasteiger, N. Yabuuchi, H. Nakanishi, J.B. Goodenough, Y. Shao-Horn, Design principles for oxygen-reduction activity on perovskite oxide catalysts for fuel cells and metal-air batteries, *Nat. Chem.* 3 (2011) 546–550.
- [43] M.C. Biesinger, B.P. Payne, A.P. Grosvenor, L.W.M. Lau, A.R. Gerson, R.S.C. Smart, Resolving surface chemical states in XPS analysis of first row transition metals, oxides and hydroxides: Cr, Mn, Fe, Co and Ni, *Appl. Surf. Sci.* 257 (2011) 2717–2730.
- [44] T. Yamashita, P. Hayes, Analysis of XPS spectra of Fe²⁺ and Fe³⁺ ions in oxide materials, *Appl. Surf. Sci.* 254 (2008) 2441–2449.
- [45] T.S. Phan, A.R. Sane, B. Rêgo de Vasconcelos, A. Nzihou, P. Sharrock, D. Grouset, D. Pham Minh, Hydroxyapatite supported bimetallic cobalt and nickel catalysts for syngas production from dry reforming of methane, *Appl. Catal. B* 224 (2018) 310–321.
- [46] M. Wang, T. Zhao, X. Dong, M. Li, H. Wang, Effects of Ce substitution at the A-site of LaNi_{0.5}Fe_{0.5}O₃ perovskite on the enhanced catalytic activity for dry reforming of methane, *Appl. Catal. B* 224 (2018) 214–221.
- [47] Y. Cao, P. Maitarad, M. Gao, T. Taketsugu, H. Li, T. Yan, L. Shi, D. Zhang, Defect-induced efficient dry reforming of methane over two-dimensional Ni/h-boron nitride nanosheet catalysts, *Appl. Catal. B* 238 (2018) 51–60.
- [48] B. Erdogan, H. Arbag, N. Yasyerli, SBA-15 supported mesoporous Ni and Co catalysts with high coke resistance for dry reforming of methane, *Int. J. Hydrogen Energy* 43 (2018) 1396–1405.
- [49] R.C. Rabelo-Neto, H.B.E. Sales, C.V.M. Inocencio, E. Varga, A. Oszko, A. Erdohelyi, F.B. Noronha, L.V. Mattos, CO₂ reforming of methane over supported LaNiO₃ perovskite-type oxides, *Appl. Catal. B* 221 (2018) 349–361.
- [50] J.N. Xin, H.J. Cui, Z.M. Cheng, Z.M. Zhou, Bimetallic Ni-Co/SBA-15 catalysts prepared by urea co-precipitation for dry reforming of methane, *Appl. Catal. a-Gen* 554

- (2018) 95–104.
- [51] Y. Cao, M. Lu, J. Fang, L. Shi, D. Zhang, Hexagonal boron nitride supported mesoSiO₂-confined Ni catalysts for dry reforming of methane, *Chem. Commun. (Camb.)* 53 (2017) 7549–7552.
- [52] Z. Bian, S. Kawi, Highly carbon-resistant Ni–Co/SiO₂ catalysts derived from phyllosilicates for dry reforming of methane, *J. Co₂ Util.* 18 (2017) 345–352.
- [53] S. Aghamohammadi, M. Haghghi, M. Maleki, N. Rahemi, Sequential impregnation vs. Sol-gel synthesized Ni/Al₂O₃–CeO₂ nanocatalyst for dry reforming of methane: effect of synthesis method and support promotion, *Mol. Catal.* 431 (2017) 39–48.
- [54] Z. Shang, S. Li, L. Li, G. Liu, X. Liang, Highly active and stable alumina supported nickel nanoparticle catalysts for dry reforming of methane, *Appl. Catal. B* 201 (2017) 302–309.
- [55] H. Wang, X. Duan, X. Liu, G. Ye, X. Gu, K. Zhu, X. Zhou, W. Yuan, Influence of tubular reactor structure and operating conditions on dry reforming of methane, *Chem. Eng. Res. Des.* 139 (2018) 39–51.
- [56] A. Karim, J. Bravo, A. Datye, Nonisothermality in packed bed reactors for steam reforming of methanol, *Appl. Catal. A Gen.* 282 (2005) 101–109.
- [57] J.-H. Kim, D.J. Suh, T.-J. Park, K.-L. Kim, Effect of metal particle size on coking during CO₂ reforming of CH₄ over Ni-alumina aerogel catalysts, *Appl. Catal. A* Gen. 197 (2000) 191–200.
- [58] V.M. Gonzalez-delaCruz, R. Pereñiguez, F. Ternero, J.P. Holgado, A. Caballero, In situ XAS study of synergic effects on Ni–Co/ZrO₂ methane reforming catalysts, *J. Phys. Chem. C* 116 (2012) 2919–2926.
- [59] R. Thalinger, M. Gocyla, M. Heggen, R. Dunin-Borkowski, M. Grünbacher, M. Stöger-Pollach, D. Schmidmair, B. Klötzer, S. Penner, Ni-perovskite interaction and its structural and catalytic consequences in methane steam reforming and methanation reactions, *J. Catal.* 337 (2016) 26–35.
- [60] K.T.C. Roseno, R. Brackmann, M.A. da Silva, M. Schmal, Investigation of LaCoO₃, LaFeO₃ and LaCo_{0.5}Fe_{0.5}O₃ perovskites as catalyst precursors for syngas production by partial oxidation of methane, *Int. J. Hydrogen Energy* 41 (2016) 18178–18192.
- [61] M.A. Peña, J.L.G. Fierro, Chemical structures and performance of perovskite oxides, *Chem. Rev.* 101 (2001) 1981–2018.
- [62] S. Rousseau, S. Lordant, P. Delichere, A. Boreave, J.P. Deloume, P. Vernoux, La(1-x)Sr_xCo_{1-y}FeyO₃ perovskites prepared by sol-gel method: characterization and relationships with catalytic properties for total oxidation of toluene, *Appl. Catal. B* 88 (2009) 438–447.